Amorphous nickel hydroxide shell tailors local chemical environment on platinum surface for alkaline hydrogen evolution reaction
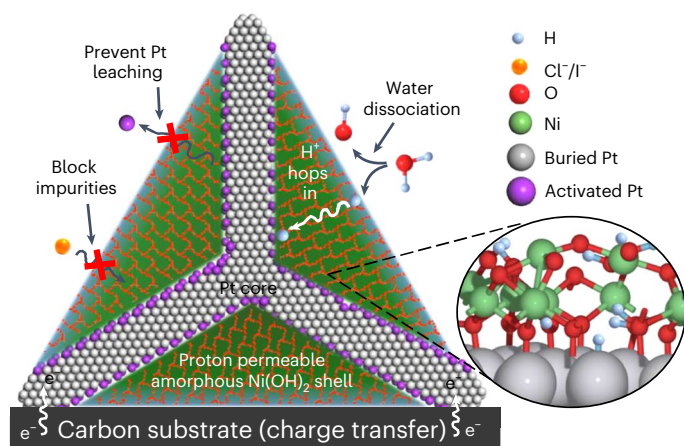
Chengzhang Wan [1,2], Zisheng Zhang[1], Juncai Dong [3], Mingjie Xu[4,5], Heting Pu[1], Daniel Baumann[1], Zhaoyang Lin[1], Sibo Wang [1], Jin Huang [2], Aamir Hassan Shah [1], Xiaoqing Pan[4,5,6], Tiandou Hu[3], Anastassia N. Alexandrova [1,2,7] ✉, Yu Huang [2,7] ✉ & Xiangfeng Duan [1,7] ✉

In analogy to natural enzymes, an elaborated design of catalytic systems with a specifically tailored local chemical environment could substantially improve reaction kinetics, effectively combat catalyst poisoning effect and boost catalyst lifetime under unfavourable reaction conditions. Here we report a unique design of 'Ni(OH)$_2$-clothed Pt-tetrapods' with an amorphous Ni(OH)$_2$ shell as a water dissociation catalyst and a proton conductive encapsulation layer to isolate the Pt core from bulk alkaline electrolyte while ensuring efficient proton supply to the active Pt sites. This design creates a favourable local chemical environment to result in acidic-like hydrogen evolution reaction kinetics with a lowest Tafel slope of 27 mV per decade and a record-high specific activity and mass activity in alkaline electrolyte. The proton conductive Ni(OH)$_2$ shell can also effectively reject impurity ions and retard the Oswald ripening, endowing a high tolerance to solution impurities and exceptional long-term durability that is difficult to achieve in the naked Pt catalysts. The markedly improved hydrogen evolution reaction activity and durability in an alkaline medium promise an attractive catalyst material for alkaline water electrolysers and renewable chemical fuel generation.

Hydrogen evolution reaction (HER) represents an essential reaction for water electrolysis that is of increasing interest for converting intermittent renewable electricity into storable hydrogen fuel. Platinum (Pt) is regarded as the best element for catalysing HER[1–4]. In particular, the Pt catalysts feature a small overpotential for HER in the acidic condition where the cathodic HER is usually regarded as a trivial challenge. However, the HER kinetics on Pt in the alkaline condition is markedly slower, with the HER rate orders of magnitude lower than that in the acidic electrolyte (Supplementary Fig. 1) due to the sluggish water dissociation (WD) and the poor proton supply rate[5–7]. Considerable efforts have been placed on tailoring the Pt active sites for improved HER kinetics. Beyond the active sites, the local chemical

Fig. 1 | 'Ni(OH)₂-clothed Pt-tetrapod' with the proton conductive amorphous Ni(OH)₂ to tailor local chemical environment on Pt surface for optimum HER in bulk alkaline electrolyte. (1) The 'Ni(OH)₂-clothed Pt-tetrapod' structure offers an ideal geometry for isolating most of the Pt surface sites from the bulk alkaline electrolyte while allowing the less encapsulated 'feet' to make robust electrical contacts with the carbon support for efficient electron transport to the catalytic sites; (2) the amorphous Ni(OH)₂ shell functions as an effective WD catalyst and a proton conductive layer to ensure efficient proton supply to the interfacial Pt sites, creating a proton-enriched local environment and fundamentally altering the HER to kinetics to the acidic-like Tafel-step limited pathway; (3) the Ni(OH)₂ shell effectively rejects impurity ions and retards Oswald ripening process, endowing a high tolerance to water impurities and long-term durability not attainable in the naked Pt catalysts.

species can compete for adsorption on active sites, inactivate (poison) the catalytic sites or profoundly affect the mass transfer of feedstocks/products[8,9]. Additionally, catalysts are inherently dynamic materials whose structures may evolve continuously during the adsorption of reactants and desorption of products, which could fundamentally affect the catalyst activity, durability and lifetime.

In general, the local chemical environment on or near the catalytic surface plays a critical role in determining the reaction pathway and kinetics. Practical water electrolysis requires a concerted supply of the reactants and removal of the products under specific operating conditions to achieve high activity, excellent tolerance to water impurities, and long lifetime. To this end, a comprehensive approach that integrates electrocatalytic active site design with rational strategies to manipulate nanoscale charge/mass transport, ion separation or structural evolution is critical for designing high-performing electrocatalysts that can facilitate efficient electron transfer and chemical transformations under practical operating conditions. This is analogous to the natural enzymes where precisely tailored micro-environment works in concert with the active site to ensure superior activity, selectivity and durability. Such an elaborate design is particularly important for alkaline water electrolysis where the local chemical environment near the active Pt sites in alkaline electrolytes is far more complex than that in an acidic electrolyte due to the limited proton supply rate, competitive adsorption of positively charged alkali metal cations (versus protons) or other undesirable strong binding impurities that could poison the catalytic sites[10].

In this Article, we report a unique design of 'Ni(OH)₂-clothed Pt-tetrapod' core/shell nanostructure [Pt$_{tet}$@Ni(OH)₂] to create a local chemical environment that can provide efficient proton (H⁺) supply to the Pt active sites and greatly boost HER performance in alkaline medium (Fig. 1). The designed [Pt$_{tet}$@Ni(OH)₂] consists of a Pt nano-tetrapod (Pt$_{tet}$) core as the HER catalyst and an amorphous Ni(OH)₂ shell as the WD catalyst and proton conductive layer to ensure abundant proton supply to the active Pt sites[11,12], fundamentally altering

the HER kinetics to the acidic-like Tafel step limited pathway and achieving a lowest Tafel slope of 27 mV per decade, a highest specific activity (SA: 27.7 mA cm$_{Pt}$⁻²) and mass activity (MA: 13.4 A mg$_{Pt}$⁻¹ at −70 mV versus reversible hydrogen electrode (RHE)) in alkaline electrolyte. Additionally, the encapsulation by Ni(OH)₂ efficiently rejects impurity ions (for example, Cl⁻ and I⁻) and suppresses Pt dissolution, leading to significantly enhanced tolerance towards halide anions and excellent durability not attainable in conventional naked Pt catalysts.

Structure characterizations of Pt$_{tet}$@Ni(OH)₂

The Pt$_{tet}$@Ni(OH)₂ nanoparticles prepared using a one-pot synthesis process (Methods) exhibit monodispersed tetrahedral shapes (Fig. 2a), with a crystalline Pt tetrapod core (Supplementary Fig. 2) encapsulated in an amorphous Ni-containing shell (Fig. 2b), and a total Pt/Ni atomic ratio of 1.0:2.3 (Supplementary Figs. 3 and 4). X-ray photoelectron spectroscopy studies show that Pt can be assigned to Pt (0) with minor Pt(II) species, while the Ni species are mainly Ni(OH)₂ (Supplementary Fig. 5)[13,14]. X-ray diffraction studies reveal face-centred cubic Pt crystalline structure (Supplementary Fig. 5), with no apparent diffraction peaks for Ni species, consistent with the amorphous nature of the Ni(OH)₂ shell[15]. Overall, the Pt-tetrapod body is well encapsulated by the amorphous Ni(OH)₂ shell and isolated from the bulk electrolyte, while the Pt-tetrapods feet (tips) are less encapsulated for robust electrical contacts with the carbon support and efficient electron transport to the catalytic sites (Fig. 1 and Supplementary Note 1).

The Fourier transform extended X-ray absorption fine structure (EXAFS) signal of Pt$_{tet}$@Ni(OH)₂ exhibits a major peak of Ni-O at 1.66 Å, and a second major peak of Ni-Ni at 2.69 Å (Fig. 2c). The corresponding intensities for the Ni−Ni peaks (second coordination sphere) are considerably lower than those of standard α-Ni(OH)₂, suggesting a high degree of structural disorder in the amorphous Ni(OH)₂ shell. Additionally, the Pt$_{tet}$@Ni(OH)₂ features a notably broader Ni−Ni peak at half maximum with a considerably larger Debye−Waller factor than that of the standard crystalline α-Ni(OH)₂ (Supplementary Table 1), consistent with its amorphous nature. The X-ray absorption near edge structure (XANES) spectra of Ni K-edge and Pt L₃-edge suggest that the oxidation state of Ni is slightly lower than +2, while that of Pt is slightly higher than 0 (Supplementary Figs. 6 and 7), indicating a partial charge transfer from Pt to the Ni(OH)₂ at the interface.

EXAFS wavelet transform (WT) analysis shows the main signal of Ni−Ni coordination in the k-space is shifted from 6.4 Å⁻¹ in standard Ni(OH)₂ to 7.0 Å⁻¹ in Pt$_{tet}$@Ni(OH)₂ (Fig. 2d), suggesting the existence of Ni-Pt coordination. This is also consistent with the negative shift of Pt−Pt k value observed in Pt-L₃ edge EXAFS-WT analysis for Pt$_{tet}$@Ni(OH)₂ (Supplementary Fig. 8). The best-fitting results show that the bonding distance of Ni−Pt coordination (3.10 Å) (Supplementary Fig. 9 and Supplementary Tables 1 and 2) is considerably larger than that in PtNi alloy (2.66 Å) (ref. 16), indicating that the Ni and Pt atoms are probably bridged by O atoms.

The acidic-like local environment on Pt surface

We next evaluated the proton accessibility of the Pt core in Pt$_{tet}$@Ni(OH)₂ by quantifying the proton-accessible electrochemical surface area (ECSA). Interestingly, the cyclic voltammetry (CV) studies reveal that the Pt$_{tet}$@Ni(OH)₂ displays an ECSA about 80% of the naked Pt$_{tet}$ (Fig. 3a), suggesting the proton permeability of the Ni(OH)₂ shell. Similar to most Pt catalysts, the naked Pt$_{tet}$ shows a notably different hydrogen adsorption/desorption CV in the alkaline versus acidic conditions (Fig. 3b)[17–19]. In contrast, the Pt$_{tet}$@Ni(OH)₂ in the alkaline electrolyte show rather similar hydrogen desorption behaviour to that of the naked Pt$_{tet}$ in the acidic electrolyte (Fig. 3c), indicating local chemical environment near the Pt sites of Pt$_{tet}$@Ni(OH)₂ in alkaline electrolyte is largely comparable that of the naked Pt in acidic environment.

The HER polarization curves of the Pt$_{tet}$@Ni(OH)₂, the naked Pt$_{tet}$ and Pt/C show nearly identical HER rates at pH 0, suggesting rapid
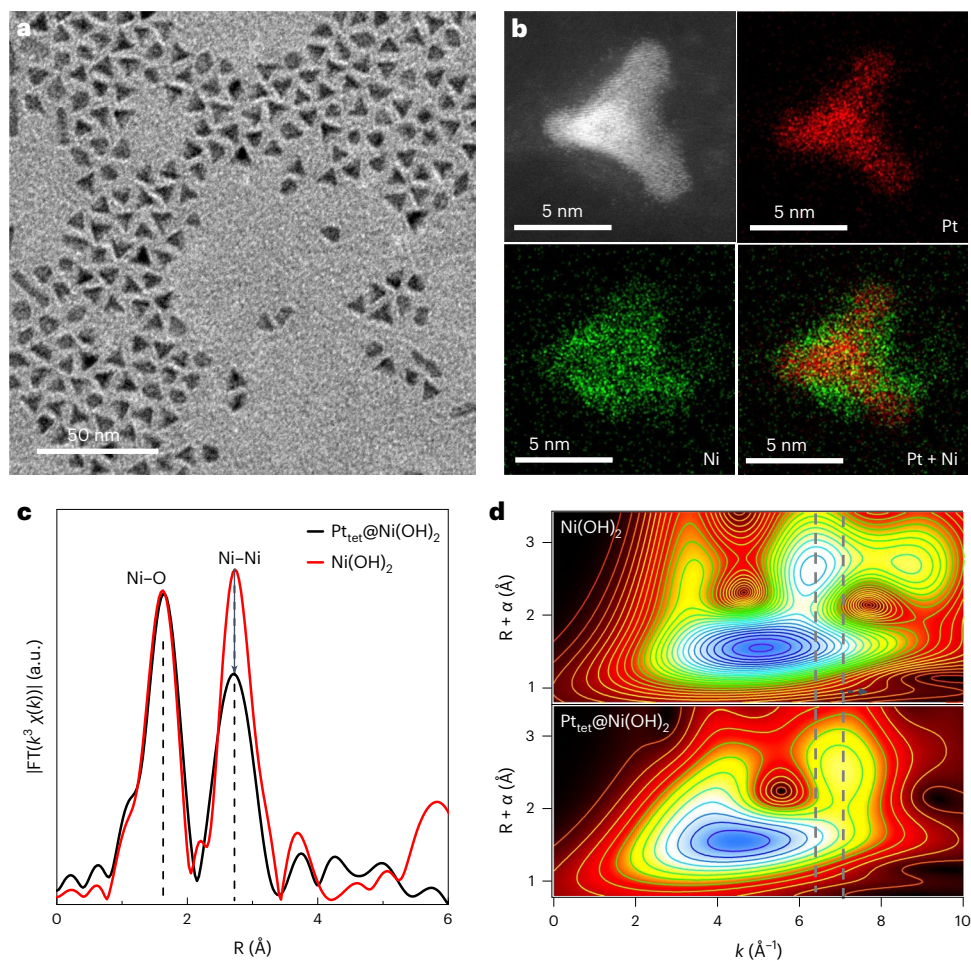
Fig. 2 | Structural characterizations of Pt$_{tet}$@Ni(OH)$_2$ nanocatalysts. a, The TEM image of Pt$_{tet}$@Ni(OH)$_2$. **b**, HAADF-STEM image of Pt$_{tet}$@Ni(OH)$_2$, and X-ray EDS mapping images of Pt, Ni and Pt + Ni. **c**, Ni K edge EXAFS-FT signals of Pt$_{tet}$@Ni(OH)$_2$ and α-Ni(OH)$_2$. The significantly lower peak intensity and broader peak width at half maximum for the Ni-Ni peak in Pt$_{tet}$@Ni(OH)$_2$ versus crystalline α-Ni(OH)$_2$ reference indicate the amorphous nature of the Ni(OH)$_2$ shell. **d**, WT for the Ni k^3-weighted EXAFS signals of α-Ni(OH)$_2$ and Pt$_{tet}$@Ni(OH)$_2$. The positive shift of the Ni-Ni coordination signal from 6.4 to 7.0 Å^{-1}) in the k-space indicates Ni is also coordinated with a heavier element, which should be Pt.

kinetics in acidic environment dictated by mass transport limitation[20]. On the other hand, notably different HER rates were observed at pH 14. In particular, the naked Pt$_{tet}$ and Pt/C feature a markedly lower HER current under pH 14 than that under pH 0 due to distinct proton supply rate (Fig. 3d), while the Pt$_{tet}$@Ni(OH)$_2$ shows a much more comparable HER polarization curve between pH 0 and 14, indicating a similar local chemical environment regardless of the entirely different bulk electrolytes. Additionally, the Pt$_{tet}$@Ni(OH)$_2$ catalysts show uninterrupted increase of the HER current during the cathodic scan (Fig. 3d), indicating that the amorphous Ni(OH)$_2$ layer is also H$_2$ permeable.

These distinct HER kinetics can further be highlighted by the Tafel slope analysis. The Pt/C, naked Pt$_{tet,}$ and Pt$_{tet}$@Ni(OH)$_2$ show a low and comparable Tafel slope of around 18–19 mV per decade at pH 0 (Fig. 3e), consistent with previous reports in the acidic environment and the well-accepted HER mechanism with the Tafel-step limited pathway (Supplementary Note 2)[21–24]. On the other hand, the Pt/C, naked Pt$_{tet}$ and Pt$_{tet}$@Ni(OH)$_2$ show distinct Tafel slopes of 75–129 mV per decade, 40–102 mV per decade and 27 mV per decade at pH 14 (Fig. 3e). The much higher Tafel slopes observed in Pt/C and Pt$_{tet}$ at pH 14 are consistent with the Volmer or Heyrovsky limited kinetics expected in the alkaline electrolyte, while the much lower Tafel slope of 27 mV per decade observed for Pt$_{tet}$@Ni(OH)$_2$ at pH 14 suggests a distinct Tafel step limited mechanism more similar to that in an acidic

environment[25–28]. Indeed, a closer comparison of the HER activity of the Pt$_{tet}$@Ni(OH)$_2$ at pH 14 with that of the Pt/C at pH 0–3 indicates that the HER kinetics of the Pt$_{tet}$@Ni(OH)$_2$ at pH 14 is comparable to that of the Pt/C at pH 1–2 (Supplementary Fig. 10).

The HER Tafel slope of 27 mV per decade achieved with the Pt$_{tet}$@Ni(OH)$_2$ is notably lower than those achieved previously with Pt or modified Pt catalysts in alkaline conditions (Fig. 3f)[2,29–34]. Although it has been well reported that the surface decoration with Ni species may facilitate the WD and partly accelerate the HER kinetics on Pt (ref. 3), most of the surface Pt sites in such decorated catalysts remain exposed to the bulk alkaline electrolyte (Supplementary Fig. 11). In this case, the protons generated from Ni-catalysed WD could be rapidly consumed within ~1 nm through re-association with the abundant hydroxide anions in alkaline electrolyte (Supplementary Note 3). Thus, only a small fraction of Pt sites in close proximity to the decorated Ni species may benefit from the improved WD kinetics (Supplementary Fig. 11), and the overall HER kinetics largely retain typical alkaline HER characteristics with an overall Tafel slope of ~40 mV per decade or higher (Supplementary Table 3). In contrast, the encapsulation of Pt surface with a proton-permeable amorphous Ni(OH)$_2$ shell in our Pt$_{tet}$@Ni(OH)$_2$ catalysts isolates most active Pt sites from alkaline electrolyte while ensuring efficient proton transfer, thus fundamentally altering the HER to acidic-like Tafel-step limited kinetics.
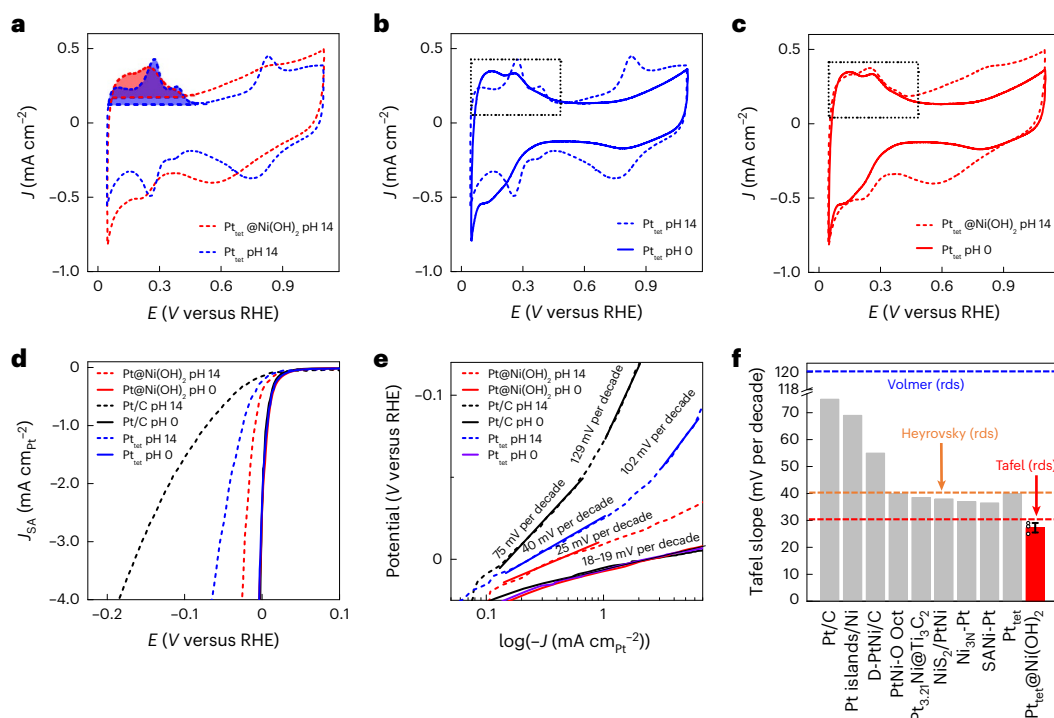
Fig. 3 | Electrochemical characterizations of $Pt_{tet}@Ni(OH)_2$ nanocatalysts.
a, The CV of the $Pt_{tet}@Ni(OH)_2$ and naked Pt_{tet} in 1.0 M KOH. The proton accessible ECSA of the $Pt_{tet}@Ni(OH)_2$ with full $Ni(OH)_2$ shell is about ~80 % of the ECSA of the naked Pt_{tet}, confirming the proton permeability of the amorphous $Ni(OH)_2$ shell. **b**, The CV curves of the naked Pt_{tet} under pH 0 and 14 show distinct characteristics in the hydrogen adsorption/desorption region. **c**, The CV curves of $Pt_{tet}@Ni(OH)_2$ under pH 0 and 14 show similar characteristics in hydrogen adsorption/desorption region, indicating a largely comparable proton supply near the Pt sites in $Pt_{tet}@Ni(OH)_2$ even in bulk alkaline electrolyte. **d**, Polarization curves (SA) of $Pt_{tet}@Ni(OH)_2$, Pt_{tet}, and Pt/C in pH 0 and 14, respectively. **e**, Tafel slopes of $Pt_{tet}@Ni(OH)_2$, Pt_{tet} and Pt/C pH 0 and 14, respectively. **f**, Comparison of

the Tafel slopes of $Pt_{tet}@Ni(OH)_2$ with the state-of-the-art alkaline HER catalysts. The dotted lines represent the Tafel slopes determined by three distinct rate-determining steps (rds): Volmer step (blue); Heyrovsky step (green) and Tafel step (red). All previous studies of Pt or modified Pt catalysts show a Tafel slope of ~40 mV per decade or above in alkaline electrolytes, consistent with a Volmer step or Heyrovsky limited mechanism, while the Tafel slope achieved with our $Pt_{tet}@Ni(OH)_2$ catalysts is below 27.3 ± 1.8 mV per decade, comparable to the typical values observed in the acidic electrolyte, suggesting abundant proton supply near the Pt surface in our unique design of $Pt_{tet}@Ni(OH)_2$ catalysts despite the bulk alkaline electrolyte. The error bars are 27.3 ± 1.8 mV per decade standard deviation with $n = 3$.

WD and proton transfer in $Pt@Ni(OH)_2$

We established an atomistic model of the $Pt/Ni(OH)_2$ interface using grand canonical genetic algorithm (GCGA) (Methods, Supplementary Figs. 12 and 13, and Supplementary Table 4). The global minimum configuration features a highly disordered NiO_xH_y ($Ni_{12}O_{25}H_{13}$) layer on Pt(111) (Fig. 4a). This disordered NiO_xH_y layer contains a flexible Ni-O framework and hydrogen bond matrix featuring a co-existence of Ni-bonded OH, adsorbed H_2O, bridging O and bridging OH^+ species (Fig. 4b), distinct from the crystalline layered double hydroxide.

The NiO_xH_y layer induces a charge transfer from Pt to NiO_xH_y, resulting in slightly positively charged interfacial Pt atoms (Supplementary Fig. 14 and Supplementary Note 4), in agreement with the XANES results. The reduced interfacial Pt electron density makes the chemisorbed *H favour the atop site. Considering the pH of the alkaline electrolyte, our calculations indicate that the ΔG_H of Pt (111) atop, Pt(111) fcc sites, and $Pt@NiO_xH_y$ atop sites are all on the right side of the Sabatier volcano and far away from the volcano top (Supplementary Fig. 15 and Supplementary Table 5), which cannot fully account for the excellent HER activity observed in experiment, and suggests additional factors at play.

Since the alkaline HER activity largely relies on the proton generation rate from WD step and the proton supply rate to the catalytic sites, we investigated the WD pathways on different NiO_xH_y sites (Fig. 4c). For the reference, WD on Pt(111) has an activation barrier of 0.92 eV and a ΔG of 0.70 eV (Fig. 4c, red). At the outer layer of NiO_xH_y, water gets dissociated at the 4-coordinated Ni, transferring one H^+ to a

neighbouring bridging O, forming a loosely held $Ni-OH^+-Ni$ bridge, with a barrier of 0.49 eV and a ΔG of 0.33 eV (Fig. 4c, green), which is similar to the WD on crystalline $Ni(OH)_2$ (Supplementary Fig. 16a). The H^+ on the bridging OH^+ could readily detach and move to other bridging O within NiO_xH_y. The OH^- remaining on the surface Ni can diffuse away from the electrode via proton exchange with nearby water molecules to initiate a new WD cycle and maintain charge balance. Deeper into the NiO_xH_y layer, water can more readily dissociate with the assistance of the H-bonding network, showing a much lower barrier of 0.19 eV (Fig. 4c, blue).

The efficient transport of protons to the interfacial Pt sites is critical for sustained HER. The NiO_xH_y features a complex H-bond network with three relevant deprotonation/protonation states including oxo, hydroxyl and adsorbed water, in which both hydroxyl/oxo and water/hydroxyl pairs can facilitate proton transfer with a rather low activation barrier of 0.02 eV (Fig. 4c) and 0.03 eV (Supplementary Fig. 17). These are in sharp contrast to the much higher barrier for intra- and inter-layer proton migration (1.09 and 0.54 eV, respectively) in crystalline $Ni(OH)_2$ (Supplementary Fig. 16b,c). Notably, in the final state of a proton transfer, the H^+ is delocalized in between the donor and acceptor O sites (Supplementary Note 5), similar to the oxonium ion ($H_5O_2^+$) (ref. 35). Therefore, at the thermodynamic equilibrium state, such delocalized protons inside NiO_xH_y may readily transfer from the NiO_xH_y/electrolyte interface to the Pt/NiO_xH_y interface following the Grotthuss-type mechanism. In this picture, the water or hydroxyl near the Pt surface dissociates to form Pt–H,
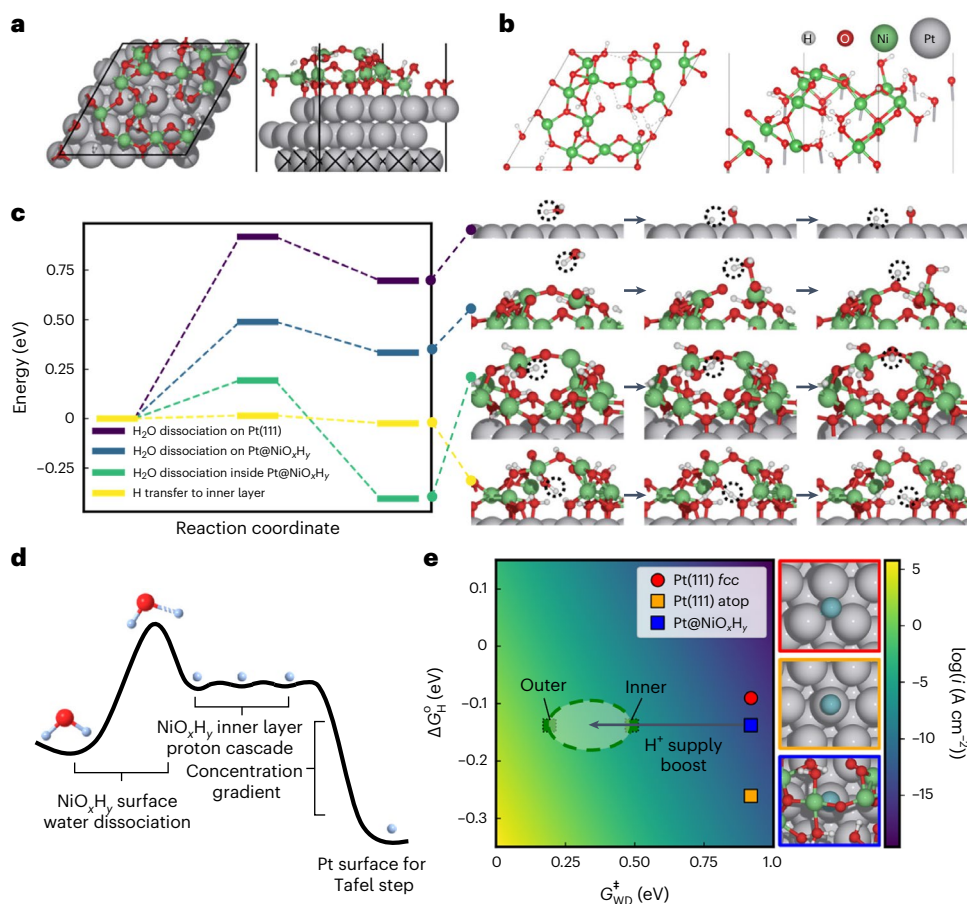
Fig. 4 | DFT calculations of the Pt@NiOxHy interface. a, The top and side views of the global minimum geometry of the disordered NiO_xH_y layer on Pt surface from the GCGA search. **b**, The hydrogen bond network in the NiO_xH_y layers. The Pt(111) substrate is hidden for clarity. **c**, Energy profiles of the WD processes on bare Pt(111), the outer surface of Pt@NiO_xH_y, inside the NiO_xH_y matrix, and the proton transfer to the inner layer. The geometries of the initial, transition and final states are shown to the right of the diagram. Note that, due to the Pt–O–Ni

linkages nearby, the *fcc* sites cannot stably host an *H as on bare Pt(111), and the atop site is the only available type on Pt covered by NiO_xH_y. **d**, The schematic of the reaction pathway on Pt@NiO_xH_y. The water dissociates at the NiO_xH_y surface to generate protons that migrate through the H-bond network in NiO_xH_y layer to reach the active Pt surface. **e**, HER activity colour map showing log(*i*) at the investigated HER sites as a function of $\Delta G^{\ddagger}$ WD and ΔG^o H. The geometries of the *H are shown on the right.

leaving a 'proton hole' (hydroxyl or oxo) in the interfacial NiO_xH_y, which drives the H^+ generated from WD at the NiO_xH_y/electrolyte interface to cascade inwards to the interfacial Pt sites through H-bond network in NiO_xH_y (Fig. 4d).

The accelerated WD kinetics, together with the proton permeability of the NiO_xH_y matrix, boosts the effective proton supply rate to the Pt surface for the later Tafel step. The activity of the Pt@NiO_xH_y system is hence substantially increased from the $10^{-11.2}$ A cm^{-2} of bare Pt(111) to the range of $10^{-6.1}$ to $10^{-1.1}$ A cm^{-2} (mixed contribution from inner and outer WD sites in NiO_xH_y, respectively) (Fig. 4e, and see method for simulation details), largely comparable to the performance of Pt(111) at pH 0 ($10^{-3.2}$ A cm^{-2}).

Although the WD kinetics of transition metal hydroxides have been suggested to explain the enhanced HER activity of Pt/transition metal oxide catalysts[3], a direct measurement of the WD steps on electrocatalyst is challenging due to the difficulties to decouple with subsequent hydrogen production steps. To elucidate the role of the amorphous Ni(OH)$_2$ shell as an efficient WD catalyst, we tested the WD activity of the Ni(OH)$_2$ shell by using bipolar membrane (BPM) electrolysis (Methods). The WD polarization curves (Supplementary Fig. 18) reveal that the BPM electrolysis with Pt$_{tet}$@Ni(OH)$_2$ needs an overpotential of only 0.18 V to reach 50 mA cm^{-2}, substantially smaller than that with no catalyst, with the naked Pt$_{tet}$ core or with crystalline

Ni(OH)$_2$ nanoplates (1.64 V, 0.97 V and 0.64 V, respectively), signifying a much faster WD kinetics of the amorphous Ni(OH)$_2$.

Electrochemical HER performance of Pt$_{tet}$@Ni(OH)$_2$

With greatly improved HER kinetics from the selective enrichment of protons by the Ni(OH)$_2$ proton sieve, the Pt$_{tet}$@Ni(OH)$_2$ catalysts show an ultrahigh SA of 27.7 mA cm$_{Pt}^{-2}$ at −70 mV versus RHE at pH 14, which is 28 times and 6 times higher than those of the Pt/C and the naked Pt$_{tet}$, respectively; and considerably higher than the previous state-of-the-art 14.8 mA cm$_{Pt}^{-2}$ (Fig. 5a)[1,2,29,32,33,36]. We note the SA achieved with Pt$_{tet}$@Ni(OH)$_2$ is also higher than that of the recently reported Pt-shell catalysts with elaborate strain engineering on Pd nanocubes[37]. Further, since the Ni(OH)$_2$ shell only moderately reduces the ECSA, such a high SA observed in Pt$_{tet}$@Ni(OH)$_2$ has directly led to a high MA of 13.4 A mg$_{Pt}^{-1}$ at −70 mV versus RHE, which is 18-fold and 4.6-fold of those of the Pt/C and the naked Pt$_{tet}$, respectively, and represent the best among the state-of-the-art Pt-based alkaline HER catalysts to our knowledge (Supplementary Table 6)[1,2,4,29,32,33,36,38–40].

The proton conductive Ni(OH)$_2$ shell could help isolate the active Pt sites from the bulk electrolyte environment and thus improve the catalytic tolerance to undesired water impurities (for example, halide anions) via Donnan exclusion effect[41]. For example, the Pt$_{tet}$@Ni(OH)$_2$
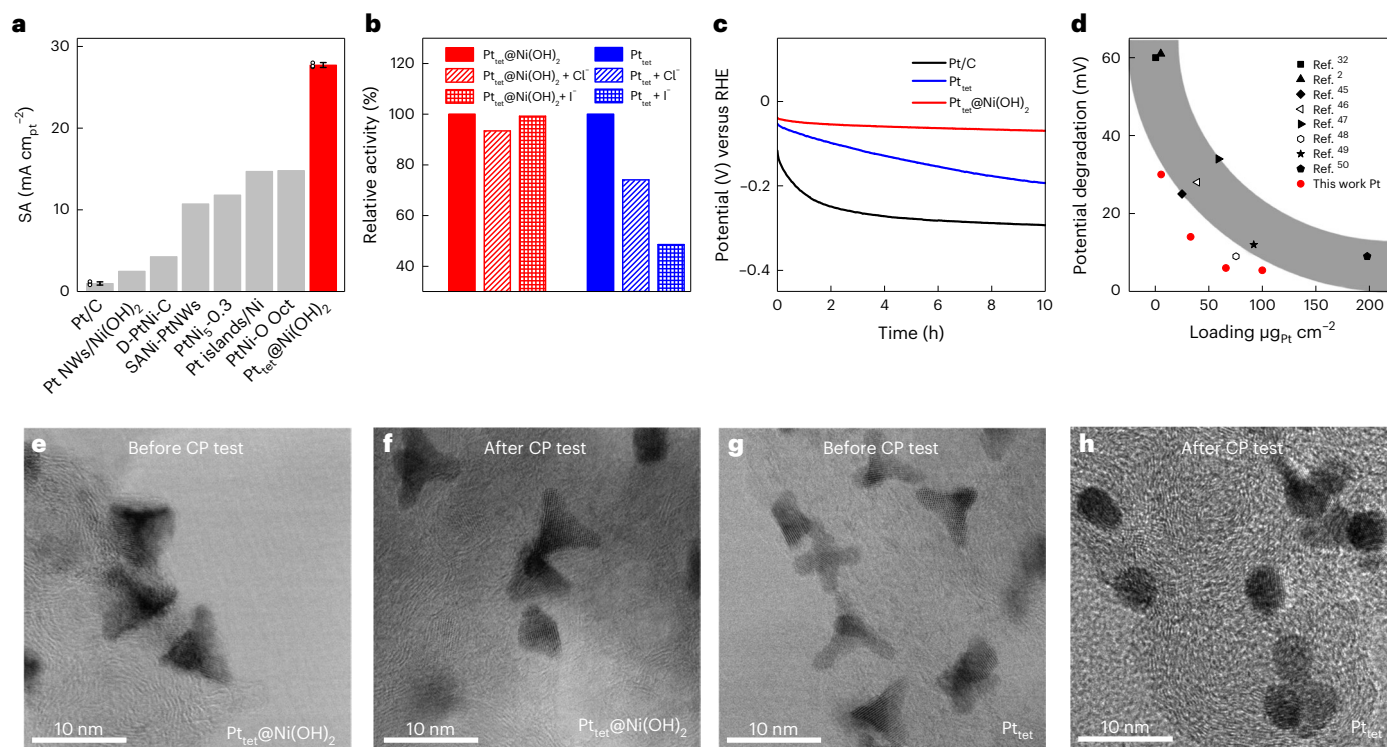
Fig. 5 | Evaluation of HER activity and stability. a, Comparison of the SA of $Pt_{tet}@Ni(OH)_2$ with the state-of-the-art alkaline HER catalysts. Error bar is added unless they are not provided in the cited literature. The error bar is 1.0 ± 0.2 mA cm_{pt}^{-2} standard deviation for Pt/C and 27.7 ± 0.3 mA cm_{pt}^{-2} standard deviation for $Pt_{tet}@Ni(OH)_2$ with $n = 3$. **b**, Relative activity of $Pt_{tet}@Ni(OH)_2$ and Pt_{tet} in pure 1.0 M KOH, 1.0 M KOH + 0.5 M Cl^- and 1.0 M KOH + 0.25 M I^-. **c**, Chronopotentiometry stability test of $Pt_{tet}@Ni(OH)_2$, Pt_{tet} and Pt/C at 10 mA cm^{-2}

(normalized by electrode geometrical area). **d**, Comparison of the stability of $Pt_{tet}@Ni(OH)_2$ with different loading with the state-of-the-art alkaline HER catalysts. Representative high-resolution transmission electron microscopy images of **e**, pristine $Pt_{tet}@Ni(OH)_2$ and **f**, $Pt_{tet}@Ni(OH)_2$ showing well retained tetrahedra shape and embeded Pt tetrapods after stability tests. **g**, pristine naked Pt_{tet} and **h**, naked Pt_{tet} showing severe ripening after the stability tests.

maintains essentially the same HER current level in the presence of 0.50 M Cl^- or 0.25 M I^- in electrolyte, while the Pt_{tet} shows a substantial current drop by 26% and 52% (Fig. 5b and Supplementary Fig. 19). Such a high tolerance to ionic impurities could help relax the water purity requirements in practical water electrolysis, which is a largely unaddressed but important issue since the ultrapure water and the relevant circulation system constitutes a significant fraction (up to 13%) of the total hydrogen production cost[42].

The Pt nanocatalysts typically feature a relatively high surface energy, and may readily undergo surface reconstruction or ripening[43,44], leading to a loss of originally designed surface structure. The encapsulation by the proton conductive $Ni(OH)_2$ shell can help retard Pt surface atom migration and dissolution to ensure high structural stability and activity durability. Our chronopotentiometry (CP) studies reveal that the $Pt_{tet}@Ni(OH)_2$ catalysts exhibit only a 30 mV overpotential increase in a 10 h continuous test (Fig. 5c), much lower than those of the naked Pt_{tet} and Pt/C (140.5 mV and 177 mV potential degradation in 10 h). A comprehensive HER durability comparison at different catalyst loading further highlights the extraordinary stability of $Pt_{tet}@Ni(OH)_2$ catalysts (Fig. 5d and Supplementary Fig. 20)[2,32,45–50]. Additionally, durability test with periodic surface cleaning reveals that the activity loss observed in the $Pt_{tet}@Ni(OH)_2$ can be largely recovered after a surface cleaning process at an oxidative potential, indicating little irreversible catalyst degradation, while the Pt_{tet} and Pt/C show much larger irreversible degradation (Supplementary Fig. 21). Detailed structural analyses confirm that the tetrahedral shape of the $Pt_{tet}@Ni(OH)_2$ and the embedded Pt tetrapods are well retained (Fig. 5e,f and Supplementary Fig. 22) with little Pt loss after the long-term durability test. In contrast, the naked Pt_{tet} without $Ni(OH)_2$ shell undergoes severe ripening with

higher Pt loss during the stability test and turns into nearly spherical nanoparticles, which contributes to more severe irreversible activity degradation (Fig. 5g,h).

In summary, we have reported a unique design of '$Ni(OH)_2$-clothed Pt-tetrapod' coreshell nanostructure, in which the amorphous $Ni(OH)_2$ shell functions as a WD catalyst and proton conductive shell to isolate the catalytic Pt surface from the bulk alkaline electrolyte while ensuring efficient proton supply to Pt sites. It delivers an acidic-like HER kinetics in bulk alkaline electrolyte, achieving the lowest Tafel slope and the highest alkaline HER activity among all Pt-based catalysts reported so far. Moreover, the encapsulation of the catalytic surface by the proton conductive shell considerably slows the dissolution/diffusion of Pt atoms from catalytic surfaces and suppresses the undesirable poisoning effect from impurity ions, thus ensuring high structural and activity durability. The markedly improved alkaline HER performance presents an attractive catalyst material for alkaline water electrolysers. Additionally, the demonstrated capability to fundamentally modify the reaction kinetics by tailoring the local chemical environment may be expanded for the design of a new generation of electrocatalysts with a favourable reaction environment and high selectivity or durability for other fundamentally and technologically important electrochemical reactions.

Online content

Any methods, additional references, Nature Portfolio reporting summaries, source data, extended data, supplementary information, acknowledgements, peer review information; details of author contributions and competing interests; and statements of data and code availability are available at https://doi.org/10.1038/s41563-023-01584-3.

References

1. Yin, H. et al. Ultrathin platinum nanowires grown on single-layered nickel hydroxide with high hydrogen evolution activity. *Nat. Commun.* **6**, 6430 (2015).

2. Zhao, Z. et al. Surface-engineered PtNi-O nanostructure with record-high performance for electrocatalytic hydrogen evolution reaction. *J. Am. Chem. Soc.* **140**, 9046–9050 (2018).

3. Subbaraman, R. et al. Trends in activity for the water electrolyser reactions on 3*d*M(Ni,Co,Fe,Mn)hydr(oxy)oxide catalysts. *Nat. Mater.* **11**, 550 (2012).

4. Liu, Z. et al. Aqueous synthesis of ultrathin platinum/non-noble metal alloy nanowires for enhanced hydrogen evolution activity. *Angew. Chem.* **130**, 11852–11856 (2018).

5. Tian, X., Zhao, P. & Sheng, W. Hydrogen evolution and oxidation: mechanistic studies and material advances. *Adv. Mater.* **31**, 1808066 (2019).

6. Zeng, K. & Zhang, D. Recent progress in alkaline water electrolysis for hydrogen production and applications. *Prog. Energy Combust. Sci.* **36**, 307–326 (2010).

7. Satyapal, S. *US Department of Energy Hydrogen and Fuel Cells Program: 2019 Annual Merit Review and Peer Evaluation Report* (National Renewable Energy Laboratory, 2020)

8. Cao, L. et al. Atomically dispersed iron hydroxide anchored on Pt for preferential oxidation of CO in H₂. *Nature* **565**, 631–635 (2019).

9. Shen, K., Chen, X., Chen, J. & Li, Y. Development of MOF-derived carbon-based nanomaterials for efficient catalysis. *ACS Catal.* **6**, 5887–5903 (2016).

10. Shah, A. H. et al. The role of alkali metal cations and platinum-surface hydroxyl in the alkaline hydrogen evolution reaction. *Nat. Catal.* **5**, 923–933 (2022).

11. Beatty, M. E. S., Chen, H., Labrador, N. Y., Lee, B. J. & Esposito, D. V. Structure–property relationships describing the buried interface between silicon oxide overlayers and electrocatalytic platinum thin films. *J. Mater. Chem. A* **6**, 22287–22300 (2018).

12. Elbaz, Y., Furman, D. & Caspary Toroker, M. Hydrogen transfer through different crystal phases of nickel oxy/hydroxide. *Phys. Chem. Chem. Phys.* **20**, 25169–25178 (2018).

13. Mansour, A. N. Characterization of β-Ni(OH)₂ by XPS. *Surf. Sci. Spectra* **3**, 239–246 (1994).

14. Peck, M. A. & Langell, M. A. Comparison of nanoscaled and bulk NiO structural and environmental characteristics by XRD, XAFS, and XPS. *Chem. Mater.* **24**, 4483–4490 (2012).

15. Nai, J., Wang, S., Bai, Y. & Guo, L. Amorphous Ni(OH)₂ nanoboxes: fast fabrication and enhanced sensing for glucose. *Small* **9**, 3147–3152 (2013).

16. Soto-Pérez, J. et al. In situ X-ray absorption spectroscopy of PtNi-nanowire/Vulcan XC-72R under oxygen reduction reaction in alkaline media. *ACS Omega* **6**, 17203–17216 (2021).

17. Rebollar, L. et al. 'Beyond adsorption' descriptors in hydrogen electrocatalysis. *ACS Catal.* **10**, 14747–14762 (2020).

18. Sheng, W. et al. Correlating hydrogen oxidation and evolution activity on platinum at different pH with measured hydrogen binding energy. *Nat. Commun.* **6**, 5848 (2015).

19. Wang, X., Xu, C., Jaroniec, M., Zheng, Y. & Qiao, S.-Z. Anomalous hydrogen evolution behavior in high-pH environment induced by locally generated hydronium ions. *Nat. Commun.* **10**, 4876 (2019).

20. Sheng, W., Gasteiger, H. A. & Shao-Horn, Y. Hydrogen oxidation and evolution reaction kinetics on platinum: acid vs alkaline electrolytes. *J. Electrochem. Soc.* **157**, B1529 (2010).

21. Podjaski, F. et al. Rational strain engineering in delafossite oxides for highly efficient hydrogen evolution catalysis in acidic media. *Nat. Catal.* **3**, 55–63 (2020).

22. Fang, S. et al. Uncovering near-free platinum single-atom dynamics during electrochemical hydrogen evolution reaction. *Nat. Commun.* **11**, 1029 (2020).

23. Li, F. et al. Balancing hydrogen adsorption/desorption by orbital modulation for efficient hydrogen evolution catalysis. *Nat. Commun.* **10**, 4060 (2019).

24. Liang, L. et al. Cobalt single atom site isolated Pt nanoparticles for efficient ORR and HER in acid media. *Nano Energy* **88**, 106221 (2021).

25. Markovića, N. M., Sarraf, S. T., Gasteiger, H. A. & Ross, P. N. Hydrogen electrochemistry on platinum low-index single-crystal surfaces in alkaline solution. *J. Chem. Soc. Faraday Trans.* **92**, 3719–3725 (1996).

26. Marković, N. M., Grgur, B. N. & Ross, P. N. Temperature-dependent hydrogen electrochemistry on platinum low-index single-crystal surfaces in acid solutions. *J. Phys. Chem. B* **101**, 5405–5413 (1997).

27. Shinagawa, T., Garcia-Esparza, A. T. & Takanabe, K. Insight on Tafel slopes from a microkinetic analysis of aqueous electrocatalysis for energy conversion. *Sci. Rep.* **5**, 13801 (2015).

28. Zheng, Y., Jiao, Y., Vasileff, A. & Qiao, S.-Z. The hydrogen evolution reaction in alkaline solution: from theory, single crystal models, to practical electrocatalysts. *Angew. Chem. Int. Ed.* **57**, 7568–7579 (2018).

29. Li, M. et al. Single-atom tailoring of platinum nanocatalysts for high-performance multifunctional electrocatalysis. *Nat. Catal.* **2**, 495–503 (2019).

30. Wang, Y., Chen, L., Yu, X., Wang, Y. & Zheng, G. Superb alkaline hydrogen evolution and simultaneous electricity generation by Pt-decorated Ni₃N Nanosheets. *Adv. Energy Mater.* **7**, 1601390 (2017).

31. Jiang, Y. et al. Coupling PtNi ultrathin nanowires with MXenes for boosting electrocatalytic hydrogen evolution in both acidic and alkaline solutions. *Small* **15**, 1805474 (2019).

32. Alinezhad, A. et al. Direct growth of highly strained Pt islands on branched Ni nanoparticles for improved hydrogen evolution reaction activity. *J. Am. Chem. Soc.* **141**, 16202–16207 (2019).

33. Chen, H. et al. Effect of atomic ordering transformation of PtNi nanoparticles on alkaline hydrogen evolution: unexpected superior activity of the disordered phase. *J. Phys. Chem. C.* **124**, 5036–5045 (2020).

34. Wang, G., Huang, X., Liao, H.-G. & Sun, S.-G. Microstrain engineered Ni_xS₂/PtNi porous nanowires for boosting hydrogen evolution activity. *Energy Fuels* **35**, 6928–6934 (2021).

35. Laasonen, K. & Klein, M. L. Structural study of (H₂O)₂₀ and (H2O)₂₁H⁺ using density functional methods. *J. Phys. Chem.* **98**, 10079–10083 (1994).

36. Zhang, C. et al. H₂ in situ inducing strategy on Pt surface segregation over low Pt doped PtNi₅ nanoalloy with superhigh alkaline HER activity. *Adv. Funct. Mater.* **31**, 2008298 (2021).

37. He, T. et al. Mastering the surface strain of platinum catalysts for efficient electrocatalysis. *Nature* **598**, 76–81 (2021).

38. Wang, P. et al. Precise tuning in platinum-nickel/nickel sulfide interface nanowires for synergistic hydrogen evolution catalysis. *Nat. Commun.* **8**, 14580 (2017).

39. Wang, P., Jiang, K., Wang, G., Yao, J. & Huang, X. Phase and interface engineering of platinum–nickel nanowires for efficient electrochemical hydrogen evolution. *Angew. Chem. Int. Ed.* **55**, 12859–12863 (2016).

40. Zhou, K. L. et al. Platinum single-atom catalyst coupled with transition metal/metal oxide heterostructure for accelerating alkaline hydrogen evolution reaction. *Nat. Commun.* **12**, 3783 (2021).

41. Sarkar, S., SenGupta, A. K. & Prakash, P. The Donnan membrane principle: opportunities for sustainable engineered processes and materials. *Environ. Sci. Technol.* **44**, 1161–1166 (2010).

42. Mayyas, A. T., Ruth, M. F., Pivovar, B. S., Bender, G. & Wipke, K. B. Manufacturing Cost Analysis for Proton Exchange Membrane Water Electrolyzers (NREL, 2019).

43. McCrum, I. T., Hickner, M. A. & Janik, M. J. First-principles calculation of Pt surface energies in an electrochemical environment: thermodynamic driving forces for surface faceting and nanoparticle reconstruction. *Langmuir* **33**, 7043–7052 (2017).

44. Horch, S. et al. Enhancement of surface self-diffusion of platinum atoms by adsorbed hydrogen. *Nature* **398**, 134–136 (1999).

45. Zhang, H. et al. Open hollow Co–Pt clusters embedded in carbon nanoflake arrays for highly efficient alkaline water splitting. *J. Mater. Chem. A* **6**, 20214–20223 (2018).

46. Xing, Z., Han, C., Wang, D., Li, Q. & Yang, X. Ultrafine Pt nanoparticle-decorated Co(OH)$_2$ nanosheet arrays with enhanced catalytic activity toward hydrogen evolution. *ACS Catal.* **7**, 7131–7135 (2017).

47. Song, H. J., Sung, M.-C., Yoon, H., Ju, B. & Kim, D.-W. Ultrafine α-phase molybdenum carbide decorated with platinum nanoparticles for efficient hydrogen production in acidic and alkaline media. *Adv. Sci.* **6**, 1802135 (2019).

48. Xie, L. et al. A Ni(OH)$_2$–PtO$_2$ hybrid nanosheet array with ultralow Pt loading toward efficient and durable alkaline hydrogen evolution. *J. Mater. Chem. A* **6**, 1967–1970 (2018).

49. Chen, Z.-J. et al. Highly dispersed platinum on Honeycomb-like NiO@Ni film as a synergistic electrocatalyst for the hydrogen evolution reaction. *ACS Catal.* **8**, 8866–8872 (2018).

50. Jang, S. W. et al. Holey Pt nanosheets on NiFe-hydroxide laminates: synergistically enhanced electrocatalytic 2D interface toward hydrogen evolution reaction. *ACS Nano* **14**, 10578–10588 (2020).

Methods

Chemicals

Platinum(II) acetylacetonate (Pt(acac)$_2$, Pt 48.0%), nickel(II) acetylacetonate (Ni(acac)$_2$, 95%), glucose, tungsten(0) hexacarbonyl (W(CO)$_6$, 97%), oleylamine (>98%), 1-octadecene (ODE, >90%), nickel(II) nitrate hexahydrate (Ni(NO$_3$)$_2$·6H$_2$O), cetrimonium bromide ([(C$_{16}$H$_{33}$)N(CH$_3$)$_3$] Br) and Nafion 117 solution (~5%) were purchased from Sigma-Aldrich. Commercial Pt/C catalyst (10 wt% Pt, and particle size ~2 nm) was purchased from Alfa Aesar. Ethanol (200 proof) was obtained from Decon Labs. Potassium hydroxide (KOH) was purchased from Fisher Chemical. All the above reagents were used as received without further purification. Carbon black (Vulcan XC-72) was received from Cabot Corporation and was annealed for 2 h under Ar gas environment at 400 °C before being used. The de-ionized water (18 MΩ cm^{-1}) was obtained from an ultrapure purification system (Milli-Q advantage A10). The Naftion 117 (PEM) and the Fumasep Fas-50 (AEM) were purchased from the Fuel cell Store.

Synthesis

In a 30 ml glass vial, 20 mg Pt(acac)$_2$, 25.6 mg Ni(acac)$_2$, 32 mg W(CO)$_6$ and 135 mg glucose were dissolved in a mixture of 3 ml oleylamine and 2 ml octadecene. The mixture was sonicated for 1 h, and the resulting homogeneous solution was kept at 80 °C for 2.5 h and then heated to 140 °C for another 8 h. After the reaction, the precipitate was centrifuged out at 20,130 g and washed by ethanol/hexane (25 ml/5 ml) three times. The final product was suspended in 10 ml cyclohexane. In a 30 ml glass vial, 30 mg carbon black (the carbon black was annealed under Ar at 200 °C for 1 h before use) was sonicated in 15 ml ethanol for 1 h. Five millilitres Pt$_{tet}$@Ni(OH)$_2$ hexane solution was then added into the carbon black/ethanol solution, and the mixture was sonicated for another 1 h. The catalysts were centrifuged out at 20,130 g and washed with cyclohexane/ethanol solution three times, followed by drying in a vacuum oven for 1 h. The Pt$_{tet}$@Ni(OH)$_2$/C were then annealed in the air at 200 °C for 2 h to fully remove the surface remaining ligands. The Pt yield is about 40%, on the scale of 6 mg$_{Pt}$ per batch. It has been scaled up to 120 mg$_{Pt}$ per batch. The crystalline Ni(OH)$_2$ nanoplates were synthesized via adding 0.5 ml 30 wt% ammonia water drop by drop into 100 ml Ni(NO$_3$) solution (10 g l^{-1}) with 0.25 g cetyltrimethyl ammonium bromide (CTAB) as the surfactant.

Characterizations

Transmission electron microscopy (TEM) images were taken on an FEI T12 operated at 120 kV. Atomic-resolution high-angle annular dark-field scanning transmission electron microscopy (HAADF-STEM) images and X-ray energy dispersive spectroscopy (EDS) mapping were taken on FEI Titan Cubed Themis G2 300 at 200 kV and JEOL Grand ARM 300CF TEM/STEM with double spherical aberration correctors operated at 300 kV. Samples for TEM measurements were prepared by dropping 10–20 µl nanoparticles dispersion in hexane on a carbon-coated copper grid (Ladd Research). Powder X-ray diffraction patterns were collected on a Panalytical X'Pert Pro X-ray Powder Diffractometer with Cu-Kα radiation. The composition of catalysts was determined by inductively coupled plasma atomic emission spectroscopy (ICP-AES, Shimadzu ICPE-9000) as well as SEM-EDS (JEOL JSM-6700F FE-SEM). X-ray photoelectron spectroscopy tests were done with Kratos AXIS Ultra DLD spectrometer.

X-ray adsorption data analysis

Ni K-edge and Pt L$_3$-edge X-ray absorption spectra were acquired under ambient conditions in fluorescence and transmission modes at beamline 1W2B of the Beijing Synchrotron Radiation Facility (BSRF), using a Si(111) double-crystal monochromator. The storage ring of BSRF was operated at 2.5 GeV with a maximum current of 250 mA in top-up mode. While the energy was calibrated using Ni/Pt foil, the incident, transmitted and fluorescent X-ray intensities were monitored by using standard ion chambers and Lytle-type detector, respectively.

XAS analysis was performed according to standard procedures using the ATHENA and ARTEMIS modules implemented in the IFEFFIT software package[51]. The EXAFS signal was first obtained by background subtraction and normalization, then the $\chi(k)$ data were Fourier-transformed to real (R) space using a Hanning window. To obtain the quantitative structural parameters around the central atoms, a least-squares curve-fitting analysis of the EXAFS $\chi(k)$ data was carried out based on the EXAFS equation in R space. The structural models were constructed on the basis of the crystal structures of Ni(OH)$_2$, with the scattering amplitudes, phase shifts and photoelectron mean free path for all paths calculated with the ab initio code FEFF 8.5 (ref. [52]).

Electrochemical measurements

To obtain a homogeneous catalyst ink, 1 mg of dried Pt$_{tet}$@Ni(OH)$_2$/C was mixed with 1 ml ethanol and sonicated for 5 min. Then, 10 µl (20 µl for stability test) of Nafion (5 wt%) was added to the solution. After sonication, 20 µl of the homogeneous ink was dropped onto a 5-mm-diameter glassy carbon electrode (0.196 cm^2, Pine Research Instrumentation). The ink was dried under ambient air before electrochemical testing.

All electrochemical tests were carried out in a three-electrode cell from Pine Research Instrumentation. The working electrode was a glassy carbon rotating disk electrode coated with corresponding catalysts. The reference electrode was a Hg/HgO electrode from CH Instrument and was calibrated in 1.0 M KOH with saturated H$_2$. A graphite rod was used as the counter electrode. CV was conducted in 1.0 M KOH and 1.0 M HClO$_4$ between 50 mV to 1,100 mV versus RHE at a sweep rate of 100 mV s^{-1}. The polarization curves were tested between −200 mV and 100 mV versus RHE at a sweep rate of 5 mV s^{-1} in 1.0 M KOH and 1.0 M HClO$_4$ with a Pt loading of 5.1 µg cm^{-2} for Pt/C and 5.6 µg cm^{-2} for Pt$_{tet}$@Ni(OH)$_2$ and Pt$_{tet}$, under a rotation speed of 1,600 r.p.m. The solution resistances were measured via impedance test. ECSA was measured through the hydrogen desorption region in N$_2$ saturated 1 M KOH. The CP test was performed under 10 mA cm^{-2} for 10 h with desired amount of loading. CP test with periodic surface cleaning was performed use the same condition as the 10 h CP test, but with a 30-cycle CV from 0.05 to 1.1 V versus RHE was performed in between two CP tests to clean the surface. The BPM test was conducted in the H-cell. The BPM was fabricated by wet pressing the Nafion 117 PEM and the Fumasep Fas-30 AEM and removing all the bubbles in between two films. When desired, the WD catalysts were pre-deposited on the PEM and the press together with AEM to form BPM with sandwiched WD-CL. The BPM electrolysis is conducted in an H-cell where a combination of AEM and PEM is used to separate the acidic HER half-cell (pH 0) and alkaline OER half-cell (pH 14). Two Pt wires are used as the cathode and anode. The Pt$_{tet}$@Ni(OH)$_2$, Pt$_{tet}$ or Ni(OH)$_2$ nanoplate were uniformly dispersed at the interface between the PEM and AEM as the WD catalysts. The standard potential required to drive WD is 0.83 V (refs. [53,54]), above which the WD current increases exponentially until reaching the mass transport limit. The stability test was performed with CP under 10 mA cm^{-2} in Ar-purged KOH for 10 h.

Computational methods: GCGA sampling

To sample the non-stoichiometric chemical subspace efficiently, we use the GCGA as implemented in our open-source Python package GOCIA (https://github.com/zishengz/gocia). The GA is an evolutionary global optimization algorithm that has been successfully applied to various fields including molecular design and structural search of gas-phase and supported clusters[55–57], and the GC feature in our program allows variation of both the compositional and geometrical degrees of freedom to explore a larger chemical space of surface restructuring and adsorbate interactions, with minimal prior knowledge[58,59]. GCGA has been employed to efficiently explore the non-stoichiometric restructuring, under a certain chemical potential, of trinary alloys, 2D materials, supported metal clusters and so on[58,60].

In the GCGA algorithm, the grand canonical free energy (grand potential) instead of the potential energy is the quantity to optimize. The grand potential is approximated by:

$$\Delta G = E(\text{slab}) - E(\text{substrate}) - \sum N_i \mu_i \qquad (1)$$

Where $E(\text{slab})$ is the electronic energy of the whole optimized slab; $E(\text{substrate})$ is the electronic energy of the Pt(111) substrate; N_i is the number of element i atoms in the adlayer; μ_i is the chemical potential of element i, which is estimated from reference species as follows:

$$\mu_{\text{Ni}} = E(\text{bulk Ni}) \qquad (2)$$

$$\mu_{\text{H}} = \frac{1}{2} E(\text{H}_2) + 2.3 k_B T \text{pH} \qquad (3)$$

$$\mu_{\text{O}} = E(\text{H}_2\text{O}) - 2\mu_{\text{H}} \qquad (4)$$

A population size of 30 and a mutation rate of 30% are chosen for the GCGA sampling. The pool of initial candidates is generated using the bond length distribution algorithm, which is a random structure generation method based on the covalent radii of the atoms[61]. A pre-optimization with Hookean potential is performed to produce reasonable starting geometries before they are fed to electronic structure method codes for local optimization and energy evaluation. Mating between the candidates alive was performed to create offspring by the split-and-splice operation[62], in which the parent slabs are cut along a random plane and then spliced together. The fitness factor is assigned to each candidate on the basis of the mating counts and the grand canonical free energy. Candidates with higher fitness are more probable to mate. The similarity check against the current population is performed before adding any new candidate to remove duplicates. Mutation of the randomly chosen offspring was performed by adding or removing an adatom or adsorbate, or by rattling the surface atoms along random vectors drawn from a normal distribution. If an offspring is too similar to its parent, its mutation rate is raised to 100%. Upon the addition of each offspring to the population, the candidate with the lowest fitness is archived to maintain the population size. The structures with detached NiO_xH_y layers or unbound water molecules are removed from the population to avoid sampling into chemically irrelevant regions of the potential energy surface (PES). A flow chart summarizing the workflow of the automated GCGA sampling is provided in Supplementary Fig. 11.

Note that the ratio of exposed surface Pt atoms (1/16 for the GM structure) may be underestimated due to sampling constraints as described in the last paragraph to focus the GCGA search direction on the interfacial structures. However, this model could well reflect (1) the interfacial structure where the Pt core and NiO_xH_y shell make the most contact and (2) the reactivity of NiO_xH_y and the hydrogen bond matrix that is still present even above the surface Pt regions that are less directly bonded to the NiO_xH_y layer.

Model set-up and density functional theory methods

The Pt surface is modelled by a four-layer 4 × 4 supercell of Pt(111) surface termination with the upper two layers relaxed as a surface region while the bottom two layers are constrained as bulk region (Supplementary Fig. 11). A vacuum of 15 Å thickness is added in the Z direction to avoid spurious interactions between periodic images. The coverage of Ni was chosen to be 12 atoms per supercell for the production run, according to the lattice parameters of Pt (2.812 Å) and Ni(OH)_2 (3.165 Å):

$$16 \text{ atoms/supercell} \times \left(\frac{2.812\text{A}}{3.165\text{A}}\right)^2 \approx 12 \text{ atoms/supercell} \qquad (5)$$

which is the estimated minimal Ni coverage to fully cover the Pt(111) at the direct interface and to capture the interfacial chemistries while not heavy sample into the Ni(OH)_2-like regions.

The local optimization and energy evaluation of the generated structures are performed with the Perdew–Burke–Ernzerhof (PBE) functional[63] and projector-augmented wave (PAW) pseudopotentials[64] using the Vienna ab initio Simulation Package (VASP) program[65–68]. D3 correction is used to account for the dispersion interactions[69], and dipole corrections are applied to remove the artificial electrostatic fields arising from asymmetric slabs in periodic boundary conditions. The convergence criteria are set to 10^{-5} (10^{-6}) eV for energy and 10^{-2} eV Å^{-1} for forces. Due to the relatively large system and sampling size, only the Γ k-point is sampled in the reciprocal space of the Brillouin zone throughout, and the cut-off energy for the kinetic energy of the plane waves was 400 eV. Reaction energies are refined at higher cut-off energy of 500 eV, a tighter convergence criterion of 10^{-6} eV, and with the implicit solvation model using the VASPsol code[70,71]. The Bader charges are calculated from the charge density output using the Bader Charge Analysis code[72].

The non-stoichiometric H/O ratio in the final $\text{Ni}_{12}\text{O}_{25}\text{H}_{13}$ model is due to the formation of Pt–O–Ni bonds that replace part of the H atoms in the simulated model, while keeping a finite number of H–O–Ni moieties near the interface. The non-crystalline NiO_xH_y has an outer layer that is not directly linked to Pt but directly interfaces with bulk electrolyte, and an inner layer representing the Pt/NiO_xH_y interface. The inner layer of NiO_xH_y is directly bonded to Pt(111) via the Ni–O–Pt bonds and occasional Ni–Pt linkages, consistent with EXAFS studies.

Calculation of adsorption free energy and activation barriers

The adsorption energy is calculated by:

$$\Delta E_{\text{H}} = E(*\text{H}) - E(*) - E(\text{H}) \qquad (6)$$

where the asterisk stands for the adsorption site. The adsorption free energy of H is calculated by:

$$\Delta G_{\text{H}}^{\text{o}} = \Delta E_{\text{H}} + \text{ZPE}(*\text{H}) - T\Delta S_{\text{H}} \qquad (7)$$

where the $(\text{ZPE} - T\Delta S_{\text{H}})$ term at room temperature is taken from literature to be +0.24 eV (ref. 73). The term is pH independent and reflects the intrinsic adsorption property of the site at standard condition.

The pH-corrected adsorption free energy of H is calculated by shifting the chemical potential of the reference state of proton by the concentration dependence of the entropy, $-k_B T \ln[\text{H}^+] = \ln 10 \, k_B T$ pH (ref. 74), which yields:

$$\Delta G_{\text{H}} = \Delta G_{\text{H}}^{\text{o}} + \ln(10) k_B T \text{pH} \qquad (8)$$

The exchange current densities i_0 are calculated from ΔG_{H} following the procedures described in ref. 23. The pre-exponential factors are treated as the same for all the elementary steps.

Since the rate-limiting step of alkaline HER is the Volmer step, the kinetics of WD is expected to induce a direct boost on the overall HER rate by controlling the rate of proton supply. Such thermochemistry-independent contribution is approximated by:

$$i' = \exp\left(-\frac{\Delta G_1^{\ddagger} - \Delta G_0^{\ddagger}}{k_B T}\right) \cdot i_0 \qquad (9)$$

where $\Delta G_0^{\ddagger}$ and $\Delta G_1^{\ddagger}$ represents the free energy barrier of the WD process on the reference system Pt(111) and other sites of interest in the restructured slab. The i' is the corrected exchange current density. The estimation assumes (1) that WD on different sites shares the same pre-exponential factor; (2) the HER rate is solely determined by the kinetics of the Volmer step, and the produced *H are consumed by Tafel step at

Pt surface within a much shorter timescale; (3) there are negligible recombination of proton and hydroxide from WD because the hydrogen permeable NiO_xH_y effectively prevents the H^+ from the recombination with the OH^-.

Data availability

References

51. Ravel, B. & Newville, M. ATHENA, ARTEMIS, HEPHAESTUS: data analysis for X-ray absorption spectroscopy using IFEFFIT. *J. Synchrotron Radiat.* **12**, 537–541 (2005).
52. Rehr, J. J. & Albers, R. C. Theoretical approaches to X-ray absorption fine structure. *Rev. Mod. Phys.* **72**, 621–654 (2000).
53. Oener, S. Z., Foster, M. J. & Boettcher, S. W. Accelerating water dissociation in bipolar membranes and for electrocatalysis. *Science* **369**, 1099–1103 (2020).
54. Tufa, R. A. et al. Bipolar membrane and interface materials for electrochemical energy systems. *ACS Appl. Energy Mater.* **4**, 7419–7439 (2021).
55. Alexandrova, A. N. & Boldyrev, A. I. Search for the LinO/+1/−1 (*n* = 5–7) lowest-energy structures using the ab initio gradient embedded genetic algorithm (GEGA). Elucidation of the chemical bonding in the lithium clusters. *J. Chem. Theory Comput.* **1**, 566–580 (2005).
56. Vilhelmsen, L. B. & Hammer, B. A genetic algorithm for first principles global structure optimization of supported nano structures. *J. Chem. Phys.* **141**, 044711 (2014).
57. Zhang, Z. & Wang, Y.-G. Molecular design of dispersed nickel phthalocyanine@nanocarbon hybrid catalyst for active and stable electroreduction of CO_2. *J. Phys. Chem. C* **125**, 13836–13849 (2021).
58. Sun, G., Alexandrova, A. N. & Sautet, P. Pt8 cluster on alumina under a pressure of hydrogen: support-dependent reconstruction from first-principles global optimization. *J. Chem. Phys.* **151**, 194703 (2019).
59. Wexler, R. B., Qiu, T. & Rappe, A. M. Automatic prediction of surface phase diagrams using ab initio grand canonical Monte Carlo. *J. Phys. Chem. C* **123**, 2321–2328 (2019).
60. Tipton, W. W. & Hennig, R. G. A grand canonical genetic algorithm for the prediction of multi-component phase diagrams and testing of empirical potentials. *J. Phys. Condens. Matter* **25**, 495401 (2013).
61. Zhai, H. & Alexandrova, A. N. Ensemble-average representation of Pt clusters in conditions of catalysis accessed through GPU accelerated deep neural network fitting global optimization. *J. Chem. Theory Comput.* **12**, 6213–6226 (2016).
62. Deaven, D. M. & Ho, K. M. Molecular geometry optimization with a genetic algorithm. *Phys. Rev. Lett.* **75**, 288–291 (1995).
63. Adamo, C. & Barone, V. Toward reliable density functional methods without adjustable parameters: the PBE0 model. *J. Chem. Phys.* **110**, 6158–6170 (1999).
64. Kresse, G. & Joubert, D. From ultrasoft pseudopotentials to the projector augmented-wave method. *Phys. Rev. B* **59**, 1758–1775 (1999).
65. Kresse, G. & Furthmüller, J. Efficient iterative schemes for ab initio total-energy calculations using a plane-wave basis set. *Phys. Rev. B* **54**, 11169–11186 (1996).
66. Kresse, G. & Furthmüller, J. Efficiency of ab-initio total energy calculations for metals and semiconductors using a plane-wave basis set. *Comput. Mater. Sci.* **6**, 15–50 (1996).
67. Kresse, G. & Hafner, J. Ab initio molecular dynamics for liquid metals. *Phys. Rev. B* **47**, 558–561 (1993).
68. Kresse, G. & Hafner, J. Ab initio molecular-dynamics simulation of the liquid-metal–amorphous-semiconductor transition in germanium. *Phys. Rev. B* **49**, 14251–14269 (1994).
69. Grimme, S., Antony, J., Ehrlich, S. & Krieg, H. A consistent and accurate ab initio parametrization of density functional dispersion correction (DFT-D) for the 94 elements H-Pu. *J. Chem. Phys.* **132**, 154104 (2010).
70. Mathew, K., Sundararaman, R., Letchworth-Weaver, K., Arias, T. A. & Hennig, R. G. Implicit solvation model for density-functional study of nanocrystal surfaces and reaction pathways. *J. Chem. Phys.* **140**, 084106 (2014).
71. Mathew, K., Kolluru, V. S. C., Mula, S., Steinmann, S. N. & Hennig, R. G. Implicit self-consistent electrolyte model in plane-wave density-functional theory. *J. Chem. Phys.* **151**, 234101 (2019).
72. Yu, M. & Trinkle, D. R. Accurate and efficient algorithm for Bader charge integration. *J. Chem. Phys.* **134**, 064111 (2011).
73. Nørskov, J. K. et al. Trends in the exchange current for hydrogen evolution. *J. Electrochem. Soc.* **152**, J23 (2005).
74. Nørskov, J. K. et al. Origin of the overpotential for oxygen reduction at a fuel-cell cathode. *J. Phys. Chem. B* **108**, 17886–17892 (2004).

Acknowledgements

Author contributions

X.D. and Y.H. designed the research. C.W. performed the synthesis, most of the structural characterizations, and electrochemical tests. J.D. and T.H. performed the XAS measurement and analysed the EXAFS and XANES data. Z.Z. and A.N.A. conducted DFT calculations. S.W., H.P., J.H. and A.H.S. assisted in the synthesis. Z.L. and D.B. assisted in the SEM-EDS and X-ray diffraction analysis. M.X. conducted the aberration-corrected STEM characterization under the supervision of X.P. The paper was co-written by C.W., X.D., J.D., Z.Z., A.N.A. and Y.H. The research was supervised by X.D., Y.H. and A.N.A. All authors discussed the results and commented on the manuscript.

Competing interests

The authors declare no competing interests.

Additional information